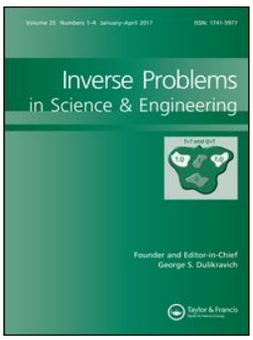

Inverse Problems in Science and Engineering

ISSN: 1741-5977 (Print) 1741-5985 (Online) Journal homepage: http://www.tandfonline.com/loi/gipe20

A homotopy method for bioluminescence tomography

R. F. Gong, X. L. Cheng & W. Han

To cite this article: R. F. Gong, X. L. Cheng & W. Han (2018) A homotopy method for bioluminescence tomography, Inverse Problems in Science and Engineering, 26:3, 398-421, DOI: 10.1080/17415977.2017.1310854

To link to this article: https://doi.org/10.1080/17415977.2017.1310854

Published online: 06 Apr 2017.

INVERSE PROBLEMS IN SCIENCE AND ENGINEERING, 2018
VOL. 26, NO. 3, 398–421
https://doi.org/10.1080/17415977.2017.1310854

Taylor & Francis
Taylor & Francis Group

A homotopy method for bioluminescence tomography

R. F. Gong[a], X. L. Cheng[b] and W. Han[c]

[a]Department of Mathematics, Nanjing University of Aeronautics and Astronautics, Nanjing, China; [b]Department of Mathematics, Zhejiang University, Hangzhou, China; [c]Department of Mathematics, University of Iowa, Iowa City, IA, USA

ABSTRACT

Bioluminescence tomography (BLT) aims at the determination of the distribution of a bioluminescent source quantitatively. The mathematical problem involved is an inverse source problem and is ill-posed. With the Tikhonov regularization, an optimization problem is formed for the light source reconstruction and it is usually solved by gradient-type methods. However, such iterative methods are often locally convergent and thus the solution accuracy depends largely on initial guesses. In this paper, we reformulate the reduced regularized optimal problem as a nonlinear equation and apply a homotopy method, which is a powerful tool for solving nonlinear problem due to its globally convergent property, to it. Numerical experiments show that the application of the homotopy technique is feasible and can produce satisfactory approximate solutions for a very large range of initial guesses.

ARTICLE HISTORY
Received 16 May 2016
Accepted 21 March 2017

KEYWORDS
Bioluminescence tomography; inverse problem; finite element methods; smoothing; homotopy method

AMS SUBJECT CLASSIFICATIONS
65F22; 65N12

1. Introduction

Recently, molecular imaging, as a rapidly developing biomedical imaging field, has been developed to study physiological and pathological processes *in vivo* at the cellular and molecular levels, see e.g. [1–5] and references therein. The goal of molecular imaging is to depict non-invasive cellular and molecular process *in vivo* sensitively and specifically, such as monitoring multiple molecular events, cell trafficking and targeting and maybe instrumental for tumorigenesis studies, cancer diagnosis, metastasis detection, drug discovery and development, gene therapies and orthopedic research [3,6–8]. In general, molecular imaging is mainly based on three technologies: nuclear imaging [9,10], magnetic resonance imaging (MRI) [11,12] and optical imaging [13,14]. Based on the three technologies, there have been a lot of models. For instance, nuclear imaging includes positron emission tomography (PET) [15–17] and single photon emission computed tomography (SPECT) [18], while optical imaging mainly involves florescence molecular tomography (FMT) [14,19] and bioluminescent imaging (BLI) [20–22]. Difference between FMT and BLI is discussed in [23]. Different technologies can also be used in a combined system [24].

Related to BLI, the Bioluminescence tomography (BLT), as one of the optical imaging modalities, has attracted much attention over the past several years because of its advantages in sensitivity and specificity. The major issue of BLT is the determination of the

CONTACT R. F. Gong grf_math@nuaa.edu.cn

distribution of a bioluminescent source. With the introduction of BLT, a bioluminescent source distribution inside a living small animal can be localized and quantified in 3D. Without BLT, bioluminescence imaging is primarily qualitative. With BLT, quantitative and localized analysis of a bioluminescent source distribution becomes feasible in a living subject [25–27]. In BLT, we reconstruct an internal bioluminescent source from the measured bioluminescent signal on the external surface of a small animal. The problem of determining the photon density on the small animal surface from the bioluminescent source distribution within the animal requires accurate representation of photon transport in biological tissue. Generally, the bioluminescent photon propagation in biological tissue can be well described by either the radiative transfer equation (RTE) or Monte Carlo model. However, at present, either model is computationally very challenging to use for most applications for that transmission of the bioluminescent photons through the biological tissue is subject to both scattering and absorption. In practice, approximation by the diffusion equation of RTE is adopted if scattering is dominant over absorption in the process of propagation of light inside a small animal [28].

In BLT, the wavelength of bioluminescent light is in the range of around or over 600nm, and in this range, scattering outperforms absorption in small animal tissue. So we can use a diffusion equation to approximate RTE. Even with this simplification, it still remains to develop efficient ways of simulating diffuse-based BLT. In this regard, we mention a few references, [25–27,29–31].

Let Ω be a domain in $\mathbb{R}^d$ ($d = 3$ for applications) with the boundary Γ, Ω_0 be a measurable subset of Ω, known as the permissible region, and χ_{Ω_0} be the characteristic function of Ω_0, i.e. its value is 1 in Ω_0 and is 0 outside Ω_0. Moreover, denote by ∂_ν the outward normal differentiation operator on Γ. Then, for known diffusion and absorption coefficients D and μ_a, the BLT problem reads as follows [25].

Problem 1.1: *Given Cauchy data g_1 and g_2, suitably smooth, find a bioluminescence source p such that (u, p) satisfies*

$$\begin{cases} -\operatorname{div}(D\nabla u) + \mu_a u = p\chi_{\Omega_0} & \text{in } \Omega, \\ D\partial_\nu u = g_1, \quad u = g_2 & \text{on } \Gamma. \end{cases} \tag{1.1}$$

As noted in [25], Problem 1.1 is ill-posed. In general, there are infinitely many solutions. When the form of the source function is pre-specified, there is no solution if the data are inconsistent. Moreover, the source function does not depend continuously on the data. To circumvent the ill-posedness, Problem 1.1 is usually studied via a regularized least-squares optimization approach.

Recently, Cheng et al. [32] proposed a coupled complex boundary method (CCBM)-based Tikhonov regularization for an inverse source problem. As is shown in [32], the CCBM makes inverse source problems more robust and more efficient in computations. Then applying the CCBM-based Tikhonov regularization, Problem 1.1 reduces to an optimization problem which is usually solved through a Newton-type iterative method. In optimal community, Newton-type methods are most popular and used frequently because of their fast convergence and simplicity. The disadvantage of Newton-type methods is the local convergence. Homotopy method is a powerful tool for solving nonlinear problem due to its globally convergent property [33]. In this paper, with Karush–Kuhn–Tucker optimization condition and adjoint equation, we reformulate the regularized optimal

problem as a nonlinear equation, which is further discretized and smoothed. Then a fixed point homotopy is applied to the reduced nonlinear system. we expect the combination of the Tikhonov regularization and homotopy technique can produce a stable and reasonable reconstruction of approximate source for a noisy measurement and a bad initial guess. As will be seen later, our new method provides good approximations to the original source function p for a very large range of initial guesses.

The rest of the paper is organized as follows. In Section 2, a CCBM-based Tikhonov regularization framework is given for a stable source function. In Section 3, the regularized optimization problem is transformed into an equivalent nonlinear equation which is discretized using FEMs. Then in Section 3.3, the reduced discrete nonlinear algebraic equation is smoothed so that the homotopy method can be applied. Several numerical examples are presented in Section 4 to demonstrate the feasibility of our method. Some concluding remarks are given in the last section.

2. Tikhonov regularization based on the CCBM

We first introduce some notation for function spaces and assumptions on the data. For a set G (e.g. Ω, Ω_0 or Γ), we denote by $H^m(G)$ the standard Sobolev spaces with inner product $(\cdot,\cdot)_{m,G}$ and norm $\|\cdot\|_{m,G}$. In particular, write $H^0(G)$ as $L^2(G)$. Let $\mathbf{H}^m(G)$ be the complex version of $H^m(G)$ with the inner product $((\cdot,\cdot))_{m,G}$ and norm $|||\cdot|||_{m,G}$ defined as follows: $\forall\, u, v \in \mathbf{H}^m(G)$, $((u,v))_{m,G} = (u,\bar{v})_{m,G}$, $|||v|||^2_{m,G} = ((v,v))_{m,G}$. The source function p will be sought from an admissible set $Q_{ad} \subset L^2(\Omega_0)$. We assume Q_{ad} is non-empty, closed and convex. For the problem data, assume Γ is Lipschitz continuous, $g_1, g_2 \in L^2(\Gamma)$, and $D, \mu_a \in L^\infty(\Omega)$, $D \geq D_0$, $\mu_a \geq \mu_0$ a.e. in Ω for some positive constants D_0 and μ_0, where $L^\infty(\Omega)$ is the space of all essentially bounded functions. In the following, we denote by c a constant which may have different values at different places.

We allow the Neumann and Dirichlet data g_1 and g_2 to contain random noise with a known level δ, and write them as g_1^δ and g_2^δ. Let

$$\|g_k^\delta - g_k\|_{0,\Gamma} \leq \delta, \quad k = 1, 2.$$

Consider a complex boundary value problem (BVP)

$$\begin{cases} -\mathrm{div}(D\,\nabla u^\delta) + \mu_a\, u^\delta = p\chi_{\Omega_0} & \text{in } \Omega, \\ D\partial_\nu u^\delta + i\, u^\delta = g_1^\delta + i\, g_2^\delta & \text{on } \Gamma, \end{cases} \tag{2.1}$$

where $i = \sqrt{-1}$ is the imaginary unit. Then Problem 1.1 is equivalent to the following inverse problem.

Problem 2.1: *Given g_1^δ and g_2^δ, find $p \in Q_{ad}$ such that*

$$u_2^\delta = 0 \quad \textit{in } \Omega,$$

where u_2^δ is the imaginary part of the solution $u^\delta = u_1^\delta + i\, u_2^\delta$ of the BVP (2.1).

We refer to [32] for the derivation of the equivalence between Problems 1.1 and 2.1.

For a given $p \in L^2(\Omega_0)$, by an application of the complex version of Lax–Milgram Lemma [34, p.376], we know that the Problem (2.1) has a unique weak solution $u \in \mathbf{H}^1(\Omega)$ and

$$|||u^\delta|||_{1,\Omega} \le c\,(\|p\|_{0,\Omega_0} + \|g_1^\delta\|_{0,\Gamma} + \|g_2^\delta\|_{0,\Gamma}). \tag{2.2}$$

We refer to [32] for the proofs of the well-posedness of (2.1) and the priori estimate (2.2).

Next we apply the Tikhonov regularization to Problem 2.1 for a stable approximation of the source function p. For any $p \in L^2(\Omega_0)$, denote by $u^\delta(p) = u_1^\delta(p) + i\,u_2^\delta(p) \in \mathbf{H}^1(\Omega)$ the weak solution of (2.1). Define an objective functional

$$J_\varepsilon^\delta(p) = \frac{1}{2}\|u_2^\delta(p)\|_{0,\Omega}^2 + \frac{\varepsilon}{2}\|p\|_{0,\Omega_0}^2,$$

and introduce the following Tikhonov regularization framework for Problem 2.1.

Problem 2.2: *Find $p_\varepsilon^\delta \in Q_{ad}$ such that*

$$J_\varepsilon^\delta(p_\varepsilon^\delta) = \inf_{p\in Q_{ad}} J_\varepsilon^\delta(p).$$

Regarding Problem 2.2, we have the following well-posedness result [32, Proposition 3.1].

Proposition 2.3: *For any $\varepsilon > 0$, Problem 2.2 has a unique solution $p_\varepsilon^\delta \in Q_{ad}$ which depends continuously on all data. Moreover, p_ε^δ is characterized by*

$$(J_\varepsilon^\delta)'(p_\varepsilon^\delta)(q - p_\varepsilon^\delta) = (w_2^\delta + \varepsilon\, p_\varepsilon^\delta, q - p_\varepsilon^\delta)_{0,\Omega_0} \ge 0 \quad \forall\, q \in Q_{ad}, \tag{2.3}$$

where w_2^δ is the imaginary part of the weak solution $w^\delta := w^\delta(p_\varepsilon^\delta) \in \boldsymbol{H}^1(\Omega)$ of the adjoint problem:

$$\begin{cases} -\mathrm{div}(D\,\nabla w^\delta) + \mu_a\, w^\delta = u_2^\delta \ \text{in } \Omega, \\ D\partial_\nu w^\delta + i\, w^\delta = 0 \qquad\qquad \text{on } \Gamma, \end{cases} \tag{2.4}$$

and u_2^δ is the imaginary part of the weak solution $u^\delta := u^\delta(p_\varepsilon^\delta) \in \boldsymbol{H}^1(\Omega)$ of the BVP (2.1) with p replaced by p_ε^δ.

Regarding the solution p_ε^δ of Problem 2.2, the following convergence result holds.

Proposition 2.4: *Denote by p^* the solution of Problem 1.1 with minimal L^2-norm. Then*

$$p_\varepsilon^\delta \to p^* \quad \text{in } L^2(\Omega_0)$$

as $\delta \to 0$, where $\varepsilon = \varepsilon(\delta)$ is chosen satisfying $\varepsilon \to 0$ and $\delta^2/\varepsilon \to 0$, as $\delta \to 0$.

Proposition 2.4 can be proved similarly to the proof of [35, Theorems 3.1], with a slight difference due to the absence of a parameter.

3. A homotopy continuity method for p_ε^δ

3.1. An equivalent nonlinear equation

To apply the homotopy technique, we transform the regularized optimal problem of Section 2 into a nonlinear equation which is further discretized with the finite element method. Note that the following discussion applies to the model with noisy measurements

g_1^δ and g_2^δ; however, for the conciseness of statements, we omit the symbol δ in most part of this section.

it is not difficult verify that for any $p, \Delta q \in L^2(\Omega_0)$,

$$J'_\varepsilon(q)\Delta q = (u_2(q), u_2(\Delta q) - u_2(0))_{0,\Omega} + \varepsilon(q, \Delta q)_{0,\Omega_0}, \tag{3.1}$$

$$J''_\varepsilon(q)(\Delta q)^2 = \|u_2(\Delta q) - u_2(0)\|^2_{0,\Omega} + \varepsilon\|\Delta q\|^2_{0,\Omega_0}, \tag{3.2}$$

where $u_2(q), u_2(\Delta q)$ and $u_2(0)$ are the imaginary parts of the weak solutions of the BVP (2.1) with p replaced by q, Δq and 0, respectively. With the similar arguments to those in [32, Proposition 3.1], we have

$$(u_2(q), u_2(\Delta q) - u_2(0))_{0,\Omega} = (w_2(q), \Delta q)_{0,\Omega_0}, \tag{3.3}$$

where $w_2(q) \in H^1(\Omega)$ is the imaginary part of the weak solution of the adjoint problem (2.4) with u_2^δ being replaced by $u_2(q)$. The Taylor expansion of $J_\varepsilon(q + \Delta q)$ at q is

$$J_\varepsilon(q + \Delta q) = J_\varepsilon(q) + J'_\varepsilon(q)\Delta q + \frac{1}{2}J''_\varepsilon(\xi)(\Delta q)^2 \tag{3.4}$$

for some $\xi \in L^2(\Omega_0)$. Then combining (3.1)–(3.4), we have

$$\lim_{\Delta q\to 0} \frac{|J_\varepsilon(q + \Delta q) - J_\varepsilon(q) - (w_2(q) + \varepsilon q, \Delta q)_{L^2(\Omega_0)}|}{\|\Delta q\|_{L^2(\Omega_0)}}$$
$$= \lim_{\Delta q\to 0} \frac{\frac{1}{2}\|u_2(\Delta q) - u_2(0)\|^2_{0,\Omega} + \frac{\varepsilon}{2}\|\Delta q\|^2_{0,\Omega_0}}{\|\Delta q\|_{L^2(\Omega_0)}} = 0$$

which shows that the Frechet derivative of J_ε at any $q \in L^2(\Omega_0)$ is

$$J'_\varepsilon(q) = \chi_{\Omega_0} w_2(q) + \varepsilon q.$$

Define a linear operator $f : L^2(\Omega_0) \to L^2(\Omega_0)$ by

$$f(q) = J'_\varepsilon(q) \quad \forall\, q \in L^2(\Omega_0).$$

In view of non-negativity of real light source function p, we set

$$Q_{ad} = \{q \in L^2(\Omega_0) \mid q \geq 0 \text{ a.e. in } \Omega_0\}.$$

Then due to Karush–Kuhn–Tucker optimization condition of Problem 2.2, there is a function $\lambda \geq 0$ such that

$$f(p_\varepsilon) - \lambda = 0, \quad \lambda p_\varepsilon = 0,$$

which gives an equivalence of linear complementary problem (LCP) to the regularized problem (Problem 2.2):

$$f(p_\varepsilon)p_\varepsilon = 0, \quad f(p_\varepsilon) \geq 0, \quad p_\varepsilon \geq 0. \tag{3.5}$$

Many papers can be consulted on the importance of LCP and its numerical solution. For a comprehensive treatment of LCP, we refer to the monograph [36].

A regularized source function p_ε^δ could be computed through the resolution of LCP (3.5). However, to have a globally convergent method for Problem 2.2, we would like to find an approximate light source function via a nonlinear equation. For this purpose, denote by Π the orthogonal projection from $L^2(\Omega_0)$ onto Q_{ad}, that is,

$$\Pi(q) = \max\{0, q\} \quad \forall\, q \in L^2(\Omega_0), \tag{3.6}$$

and define $F(q) := q - \Pi(q - f(q))$. Then, according to Harker and Pang [37], LCP (3.5) is equivalent to the following nonlinear equation:

$$F(p_\varepsilon^\delta) = 0. \tag{3.7}$$

Note that the relations in (3.5) and (3.7) are interpreted pointwisely.

3.2. Discretization with the finite element method

We apply the finite element method to discretize (3.7), and later in Subsection 3.4, use the homotopy method to solve the discretized problem. Let $\{\mathcal{T}_h\}_h$ be a regular family of finite element partitions of $\overline{\Omega}$ with meshsize h such that each element at the boundary Γ has at most one non-straight face (for a three-dimensional domain) or side (for a two-dimensional domain). Define the linear finite element space

$$V^h = \{v \in C(\overline{\Omega}) \mid v \text{ is linear in } T\ \forall\, T \in \mathcal{T}_h\}$$

for the weak solutions of (2.1) and (2.4) and

$$Q^h = \{q \in L^2(\Omega_0) \mid q \text{ is constant in } T,\ \forall\, T \in \mathcal{T}_h \text{ and } T \subset \overline{\Omega}_0\}$$

for the source function p_ε^δ. Set $\mathbf{V}^h = V^h \oplus iV^h$ and $Q_{ad}^h = Q^h \cap Q_{ad}$. Then $\mathbf{V}^h$ is a finite element subspace of $\mathbf{H}^1(\Omega)$.

For a triangulation $\mathcal{T}_h$, let n_0 be the number of elements over $\overline{\Omega}_0$, associated with elements T_k, $1 \le k \le n_0$. Assume χ_{T_k} are the characteristic functions over T_k, $1 \le k \le n_0$. Then the finite element approximation of p_ε^δ has the form

$$p^h = \sum_{s=1}^{n_0} p_k \chi_{T_k}. \tag{3.8}$$

Set $P = (p_1, p_2, \ldots, p_{n_0})^t$, where the superscript t stands for transposition. Then the finite element discretization of f, denoted by $\mathbf{f}$, is

$$\mathbf{f}(P) = M P + N \quad \forall\, P \in \mathbb{R}^{n_0}, \tag{3.9}$$

where M is an $n_0 \times n_0$ matrix which depends on Ω, Ω_0, $\mathcal{T}_h$, D, μ_a and ε, while N is an $n_0 \times 1$ vector which depends on Γ, $\mathcal{T}_h$, g_1^δ and g_2^δ. A detailed derivation of M and N are given in Appendix 1.

Correspondingly, the nonlinear Equation (3.7) reduces to solving the following system of algebraic equations:

$$\mathbf{F}(P) := P - \Pi(P - \mathbf{f}(P)) = 0. \tag{3.10}$$

Note that Π is used as a non-negative projection for both continuous and discrete functions.

Since (3.10) is equivalent to a convex problem in $\mathbb{R}^{n_0}$, it is not difficult to see that there is a unique solution P. Moreover, by [32, Theorem 4.4],

$$\|p^h - p_\varepsilon^\delta\|_{0,\Omega_0} \le c\,(\varepsilon^{-1}\,h^2 + \varepsilon^{-1/2}\,h^{1/2}\,E^h(p_\varepsilon^\delta)^{1/2}), \tag{3.11}$$

where $E^h(p_\varepsilon^\delta) = \inf_{q^h \in Q_{ad}^h} \|q^h - p_\varepsilon^\delta\|_{0,\Omega_0}$ and p^h is defined from P through (3.8).

3.3. Smoothness

Note that Π is piecewise smooth and $\mathbf{F}$ is a semismooth function. To apply the homotopy method, the operator $\mathbf{F}$ needs to be smoothed. In fact, for a real number x,

$$\Pi(x) = \max\{x, 0\} = \int_{-\infty}^{x} \sigma(t)\mathrm{d}t$$

with $\sigma(x)$ being the step function

$$\sigma(x) = \begin{cases} 1 \text{ if } x > 0, \\ 0 \text{ if } x \le 0. \end{cases}$$

Define

$$\sigma_\tau(x) = \frac{1}{1 + e^{-x/\tau}}, \quad \tau > 0$$

and

$$\Pi_\tau(x) = \int_{-\infty}^{x} \sigma_\tau(t)\mathrm{d}t = x + \tau \ln(1 + e^{-x/\tau}). \tag{3.12}$$

For properties of the operator Π_τ, the following result holds [38, Proposition 2.2].

Proposition 3.1: *Let $\tau > 0$ and $x \in \mathbb{R}$.*

(1) $0 \le \Pi_\tau(x) - \Pi(x) \le \tau \ln 2$. *Thus,*

$$\lim_{\tau \to 0^+} \Pi_\tau(x) = \Pi(x).$$

(2) $0 < \Pi_\tau'(x) < 1$. *Thus, Π_τ is a contraction mapping.*

(3) $\Pi_\tau''(x) > 0$. *Thus, Π_τ is strictly convex.*

Thanks to (1) of Proposition 3.1, we have the following smooth approximation to Equation (3.10):

$$\mathbf{F}_\tau(P) = 0, \tag{3.13}$$

where $\mathbf{F}_\tau(P) := P - \Pi_\tau(P - \mathbf{f}(P))$.

Remark 1: Note that the projection Π has the form: $\Pi(x) = \frac{1}{2}(x + |x|)$. Alternatively, we can use the conventional smoothing operator $\Pi_\tau(x) = \frac{1}{2}(x + \sqrt{x^2 + \tau^2})$. We also

implement numerical examples of Section 4 for this choice of Π_τ. Numerical results indicate that the two choices of Π_τ produce solutions of comparable accuracy, with (3.12) leading to a slightly more accurate solution.

Because $\mathbf{f}$ is linear, by Proposition 3.1, Equation (3.13) admits a unique solution P_τ which converges to P_*, the solution of (3.10):

$$\lim_{\tau \to 0^+} P_\tau = P_*. \tag{3.14}$$

Some properties of the operator $\mathbf{F}_\tau$ are summarized as follows.

Proposition 3.2:

(1) *For any* $P \in \mathbb{R}^{n_0}$,

$$\|\boldsymbol{F}_\tau(P) - \boldsymbol{F}(P)\|_l \le c_l\, \tau \ln 2$$

with $l = 1, 2, \infty$ *and* $c_1 = n_0$, $c_2 = \sqrt{n_0}$, $c_\infty = 1$.

(2) *For any* $P \in \mathbb{R}^{n_0}$, *define an* n_0 *dimensional matrix* $D(P) = (d_{ij})$ *with* $d_{ij} = 0$ *for* $j \ne i$ *and*

$$d_{ii} = \frac{e^{-\frac{p_i - (\boldsymbol{f}(P))_i}{\tau}}}{1 + e^{-\frac{p_i - (\boldsymbol{f}(P))_i}{\tau}}}.$$

Then

$$\frac{\partial \boldsymbol{F}_\tau(P)}{\partial P} = M + D(P)(E - M), \tag{3.15}$$

$$\frac{\partial \boldsymbol{F}_\tau(P)}{\partial \tau} = -\frac{1}{\tau} D(P)(P - \boldsymbol{f}(P)) - \ln\left(1 + e^{-\frac{P - \boldsymbol{f}(P)}{\tau}}\right), \tag{3.16}$$

where E *is the* n_0 *dimensional identity matrix.*

3.4. Homotopy continuity methods

Given a simple map $\mathbf{G} : \mathbb{R}^{n_0} \to \mathbb{R}^{n_0}$ such that it is easy to solve the equation $\mathbf{G}(P) = 0$, we construct a linear homotopy $H_\tau(P, \gamma)$ between the smoothing map $\mathbf{F}_\tau$ and $\mathbf{G}$ as follows:

$$H_\tau(P, \gamma) = (1 - \gamma)\, \mathbf{F}_\tau(P) + \gamma\, \mathbf{G}(P) = 0.$$

Then, $H_\tau(P, 1) = \mathbf{G}(P)$, $H_\tau(P, \gamma) \to \mathbf{F}_\tau(P)$ as $\gamma \to 0^+$. With the choice $\mathbf{G}(P) = P - P^0$, we have the following fixed point homotopy:

$$H_\tau(P, \gamma) = (1 - \gamma)\, \mathbf{F}_\tau(P) + \gamma\, (P - P^0) = 0, \tag{3.17}$$

with $P^0 \in \mathbb{R}^{n_0}$ an arbitrary non-negative initial vector. Combine (3.15) and (3.17) to give

$$\frac{\partial H_\tau}{\partial P} = (1 - \gamma) \frac{\partial \mathbf{F}_\tau(P)}{\partial P} + \gamma E,$$

$$\frac{\partial H_\tau}{\partial \gamma} = P - P^0 - \mathbf{F}_\tau(P).$$

In case $\text{Rank}(\frac{\partial H_\tau}{\partial P}) = n_0$ for any $P \in \mathbb{R}^{n_0}$, by the implicit theorem, (3.17) determines implicitly an n_0 dimensional vector function $P_\tau = P_\tau(\gamma)$, $\gamma \in (0, 1]$ such that

$$P'(\gamma) = -\left[\frac{\partial H_\tau}{\partial P}\right]^{-1} \frac{\partial H_\tau}{\partial \gamma} \triangleq f_\tau(P, \gamma). \tag{3.18}$$

Apparently, $P(1) = P^0$.

Being an affine function, **f** is smooth. We have the following result [39].

Proposition 3.3: *For fixed $\tau > 0$ and almost all $P^0 \in \mathbb{R}^{n_0}$, the homotopy Equation (3.17) determines a bounded smooth curve $C \subset \mathbb{R}^{n_0} \times (0, 1]$ starting from $(P^0, 1)$ and approaches the hyperplane at $\gamma = 0$. Moreover,*

$$\lim_{\gamma \to 0^+} P(\gamma) = P_\tau, \tag{3.19}$$

where P_τ is the unique solution of (3.13).

Recall that P_* is the unique solution of the discrete Problem (3.10). Combine (3.14) and (3.19) to give

$$\lim_{\tau \to 0^+} \lim_{\gamma \to 0^+} P(\gamma) = P_*. \tag{3.20}$$

Due to (3.20), we reduce the problem of finding an approximate light source to the one of solving an initial value problem for a sufficiently small $\tau > 0$ and $\gamma \in (0, 1]$:

$$\begin{cases} P'(\gamma) = f_\tau(P, \gamma), \\ P(1) = P^0. \end{cases} \tag{3.21}$$

Any convergent iterative method can be used to solve (3.21) numerically. For example, an explicit fourth order Runge–Kutta method for it reads:

$$\begin{aligned}
P^{(0)} &= P^0; \\
&\text{for } k = 1, 2, \ldots, m-1, \\
y_1 &= f_\tau(P^{(k-1)}, \gamma_{k-1}), \\
y_2 &= f_\tau(P^{(k-1)} + \frac{\bar\gamma}{2} y_1, \gamma_{k-1} + \frac{\bar\gamma}{2}), \\
y_3 &= f_\tau(P^{(k-1)} + \frac{\bar\gamma}{2} y_2, \gamma_{k-1} + \frac{\bar\gamma}{2}), \\
y_4 &= f_\tau(P^{(k-1)} + \bar\gamma y_3, \gamma_k), \\
P^{(k)} &= P^{(k-1)} + \frac{\bar\gamma}{6}(y_1 + 2y_2 + 2y_3 + y_4),
\end{aligned}$$

where $\bar\gamma = -1/m$ and $\gamma_k = 1 + k\bar\gamma$, $k = 0, 1, \ldots, m$, is a partition of the interval $[0, 1]$. Then $P^{(m-1)}$ is viewed as an approximation to the true source function P_*. To avoid direct computation of the inverse of matrix $\frac{\partial H_\tau}{\partial P}$, we apply the biconjugate gradients method (BICG) [40] to compute $f_\tau(P, \gamma)$. Then the explicit fourth order Runge–Kutta method is implemented by the following iterative scheme.

Algorithm 3.4:

(1) Give $\varepsilon, \tau, m, P^0$, let $P_\tau^{(0)} = P^0$ and set $k = 1$.

(2) Compute $A_1 = \frac{\partial H_\tau}{\partial P}(P^{(k-1)}, \gamma_{k-1})$, $b_1 = -\frac{\partial H_\tau}{\partial \gamma}(P^{(k-1)}, \gamma_{k-1})$ and solve $A_1 y_1 = b_1$ with BICG to get y_1.
(3) Compute $A_2 = \frac{\partial H_\tau}{\partial P}(P^{(k-1)} + \frac{\bar\gamma}{2} y_1, \gamma_{k-1} + \frac{\bar\gamma}{2})$, $b_2 = -\frac{\partial H_\tau}{\partial \gamma}(P^{(k-1)} + \frac{\bar\gamma}{2} y_1, \gamma_{k-1} + \frac{\bar\gamma}{2})$ and solve $A_2 y_2 = b_2$ with BICG to get y_2.
(4) Compute $A_3 = \frac{\partial H_\tau}{\partial P}(P^{(k-1)} + \frac{\bar\gamma}{2} y_2, \gamma_{k-1} + \frac{\bar\gamma}{2})$, $b_3 = -\frac{\partial H_\tau}{\partial \gamma}(P^{(k-1)} + \frac{\bar\gamma}{2} y_2, \gamma_{k-1} + \frac{\bar\gamma}{2})$ and solve $A_3 y_3 = b_3$ with BICG to get y_3.
(5) Compute $A_4 = \frac{\partial H_\tau}{\partial P}(P^{(k-1)} + \bar\gamma y_3, \gamma_k)$, $b_4 = -\frac{\partial H_\tau}{\partial \gamma}(P^{(k-1)} + \bar\gamma y_3, \gamma_k)$ and solve $A_4 y_4 = b_4$ with BICG to get y_4.
(6) Compute $P^{(k)} = P^{(k-1)} + \frac{\bar\gamma}{6}(y_1 + 2y_2 + 2y_3 + y_4)$.
(7) Set $k = k + 1$ and repeat Steps (2)–(6) until $k = m - 1$.

As illustrated by the numerical experiments in Section 4, the solution accuracy can be improved when an updated P^0 is used. Specifically, we will use the following iterative scheme for the homotopy-based reconstruction.

Algorithm 3.5:

(1) Give $\varepsilon, \tau, m, P_0$ and n, set $j = 0$.
(2) For $P^0 = P_j$, apply Algorithm 3.4 to get $P_j^{(m-1)}$.
(3) Set $P_{j+1} = P_j^{(m-1)}$ and $j = j + 1$, and go to Step (2) until $j = n$.

4. Numerical examples

In this section, we report some numerical results to confirm that the combination of Tikhonov regularization method and homotopy method can produce a satisfactory approximation to the true light source even for very bad initial guess.

With the problem domain Ω, Neumann data g_1, diffusion and absorption coefficients D and μ_a, and a prescribed true source function p_* in $\Omega_0 \subset \Omega$, using the standard linear finite element method defined in Subsection 3.2, we solve the forward BVP

$$\begin{cases} -\mathrm{div}(D\nabla u) + \mu_a u = p_* \chi_{\Omega_0} & \text{in } \Omega, \\ D\partial_\nu u = g_1, & \text{on } \Gamma \end{cases} \tag{4.1}$$

to get $u^h \in V^h$. Use $g_2 = u^h|_\Gamma$ for the boundary measurement. Uniformly distributed noises with level δ are added to both g_1 and g_2 to get g_1^δ and g_2^δ:

$$g_k^\delta(x) = [1 + \delta \cdot (2\,\mathrm{rand}(x) - 1)]\, g_k(x), \quad x \in \Gamma, \quad k = 1, 2,$$

where $\mathrm{rand}(x)$ returns a pseudo-random value drawn from a uniform distribution on $[0, 1]$.

With computed data g_1^δ and g_2^δ and specific parameters ε, the forward BVP (2.1) and its adjoint (2.4) are solved with the finite element method (see Section 3.2 for details) to produce M and N with which the operators $\mathbf{f}$ in (3.9) and $\mathbf{F}$ in (3.10) are defined. As a result, for $\tau > 0$ and $\gamma \in (0, 1]$, nonlinear operators $\mathbf{F}_\tau$ of (3.13) and H_τ of (3.17) are obtained. Then given additional initial guess P_0 and iteration numbers m, n, Algorithm 3.5

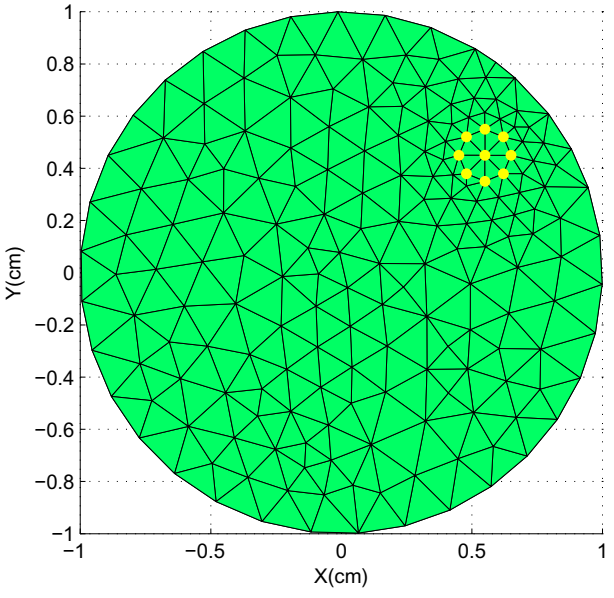

Figure 1. A sketch of Delaunay elements.

is implemented to get P_n. Through the formula (3.8), that is,

$$p^h = \sum_{k=1}^{n_0} P_{n,k} \chi_{T_k},$$

we obtain an approximation p^h to the true source function p_*. To assess the accuracy of approximate solutions, we define the L^2-norm relative error in an approximate solution p^h:

$$\text{L2Err} := \frac{\|p^h - p_*\|_{0,\Omega}}{\|p_*\|_{0,\Omega}}.$$

We note that the values of the regularization parameter ε for the numerical results in all tables below are approximately optimal. Because the true source p_* is known in our experiments, all approximate optimal regularization parameters are chosen by sweeping them from $1, 10^{-1}, 10^{-2}, 10^{-3}, \ldots$. When p_* is not available, many methods such as discrepancy principle (DP), L-curve rule, quasi-optimality, monotone error rule, generalized cross-validation (GCV) can be used for proper selection of ε. We refer to [41,42] for some further comments on these methods for the choice of the regularization parameters.

Example 1: Let $\Omega \subset \mathbb{R}^2$ be a unit circle centered at the origin. The diffusion and absorption parameters for the homogenous media Ω are $D = 0.2$ and $\mu_a = 0.04$. The Neumann data on the boundary Γ is $g_1 = (x^2 + y^2)/5$. Set the true light source $p_* = 1 + x + y$ in a circle contained in Ω, with the center $(0.55, 0.45)$ and the radius 0.1. Delaunay elements are used for the triangulations. See Figure 1 for a sketch of a mesh. The Dirichlet data g_2^δ is computed on a rather small meshsize h ($h = 0.03747$ with 44,185 nodes and 87,808 elements in our experiments), polluted by a noise with level δ.

Table 1. The dependence of the accuracy in solutions on parameters τ, m, n.

τ	L2Err	m	L2Err	n	L2Err
1	1.3199	10	2.0796	1	3.8232e−1
1/2	3.3754e−1	50	2.4254e−1	5	1.2582e−1
$1/2^2$	3.7481e−2	100	1.8659e−1	10	7.3854e−2
$1/2^3$	1.2101e−2	500	1.4593e−1	20	1.2101e−2
$1/2^4$	1.2148e−2	1000	1.0509e−1	30	3.0295e−2
$1/2^5$	1.2148e−2	1500	7.2477e−2	40	4.8678e−2
$1/2^6$	1.2148e−2	2000	4.6469e−2	50	5.8671e−2
$1/2^7$	1.2148e−2	2500	2.6079e−2	60	6.4027e−2
$1/2^8$	1.2148e−2	3000	1.2101e−2	70	6.6890e−2
$1/2^9$	1.2148e−2	3500	1.2139e−2	80	6.8421e−2
$1/2^{10}$	1.2148e−2	4000	2.0801e−2	90	6.9242e−2
$1/2^{11}$	1.2148e−2	4500	2.9193e−2	100	6.9684e−2

Table 2. The corresponding computational time (s).

τ	Time	m	Time	n	Time
1	22.52	10	1.64	1	2.50
$1/2^1$	22.53	50	2.52	5	6.55
$1/2^2$	21.86	100	2.25	10	11.09
$1/2^3$	21.88	500	5.20	20	21.88
$1/2^4$	21.91	1000	8.19	30	30.13
$1/2^5$	21.77	1500	11.45	40	39.61
$1/2^6$	21.55	2000	14.64	50	50.84
$1/2^7$	22.20	2500	18.22	60	59.25
$1/2^8$	21.77	3000	21.88	70	68.30
$1/2^9$	22.02	3500	23.78	80	78.91
$1/2^{10}$	22.50	4000	26.92	90	87.84
$1/2^{11}$	22.92	4500	31.44	100	97.06

Then using Algorithm 3.5, the approximate source function p^h is recovered on a mesh with $h = 0.1154$, for different parameters δ, ε, τ, m and n. We first investigate the effect of the smoothing parameter τ, the partition parameter m and the iteration parameter n. To this end, we fix $\delta = 0, \varepsilon = 10^{-5}$, and set $P_0 = 10$, which is totally different from the true solution p_*. The relative L^2-norm error L2Err in approximate solutions for different values of the smoothing parameter τ are given in the first two columns (fix $m = 3000$, $n = 20$); those for different values of the partition parameter m are listed in the third and forth columns (fix $\tau = 1/2^3$, $n = 20$); those for different values of the iteration parameter n are listed in the last two columns (fix $\tau = 1/2^3$, $m = 3000$). The first two columns of Table 1 show that a small τ (< 1) is readily to give a satisfactory approximate solution; the accuracy in approximate solutions are uniform with respect to a small enough τ. The third and forth columns of Table 1 show that when refining the partition of $(0, 1]$ for γ, the accuracy in approximate solutions increases at first and then decreases. A big enough m can provide a good reconstruction. The last two columns show that updating the initial guess P_0 in fixed point homotopy (3.17) can improves largely the accuracy in approximate solutions. However, too big n is not necessary. In summary, we conclude from Table 1 that a moderately small τ, a moderately big n and a big enough m produce a reasonable approximation p^h to the true source function p_*.

Table 3. The dependence of solution accuracy on δ.

δ	HM	LMLS	SQPM	IPM
0	1.2101e−2	2.4144e−2	1.4272e−2	2.9554e−2
0.1%	4.0857e−2	4.1660e−2	3.9243e−2	2.8732e−2
0.5%	3.1800e−2	3.1965e−2	1.0847e−1	6.7209e−2
1%	5.7984e−2	5.8747e−2	6.5535e−2	2.5203e−2
5%	3.7559e−1	3.7704e−1	1.8012e−1	4.9983e−1

Table 4. The corresponding computational time (s).

δ	HM	LMLS	SQPM	IPM
0	21.88	1.72	101.38	157.25
0.1%	22.67	1.55	32.41	79.92
0.5%	22.89	1.59	27.73	82.52
1%	22.67	1.55	55.84	82.56
5%	22.61	1.53	34.98	82.58

The computational time corresponding to each reconstruction is given in Table 2. Using these data and applying least square fitting, the explicit dependence of the computational time on the parameters τ, m and n are approximated in the following:

$$\text{Time}(\tau, m, n) \approx 0.006438m + 0.9587n - 16.3704.$$

We next investigate the stability of approximate solutions with respect to the noise level δ. Specifically, set $\delta = 0$, 0.1%, 0.5%, 1%, 5% and implement Algorithm 3.5 repeatedly, again for $P_0 = 10$ and over a mesh with $h = 0.1154$. As indicated by Table 1, we set $\tau = 1/8$, $m = 3000$ and $n = 20$. The approximate optimal values of the regularization parameter are $\varepsilon = 10^{-5}, 10^{-4}, 10^{-4}, 10^{-4}, 10^{-3}$. The relative errors in L^2-norm are listed in the second column of Table 3. For comparison, we list the results for $\gamma = 0$ in the third column of Table 3. Note that when $\gamma = 0$, we are reduced to solve (3.13). In our experiments, least square method and Levenberg–Marquardt method are used to solve (3.13), and the corresponding $\varepsilon = 10^{-4}, 10^{-4}, 10^{-4}, 10^{-4}, 10^{-3}$. Moreover, we list in the third and forth columns of Table 3 the results obtained by applying directly sequential quadratic programming method and primal-dual interior point method to the regularized optimal problem, respectively. For convenience, we use 'HM' to refer to homotopy method developed in this paper, 'LMLSM' refer to Levenberg–Marquardt based least square method, 'SQPM' refer to sequential quadratic programming method and 'IPM' refer to primal-dual interior point method. The approximate optimal regularization parameters for SQPM and PDIPM corresponding to different δ are $\varepsilon = 10^{-2}$, 10^{-1}, 1, 1, 1 and $\varepsilon = 10^{-1}$, 10^{-1}, 1, 10^{-1}, 10^{-4}, respectively. The corresponding computational time are shown in Table 4. Table 3 shows that all four methods are stable and can give satisfactory reconstructions. In comparison, homotopy method explored in this paper has better solution accuracy than other three methods. About the computational efficiency, Table 4 indicates that Levenberg–Marquardt based least square method is faster than other three methods, and HM is faster than SQPM and IPM.

Finally, we assess the convergence behavior of our homotopy method with respect to initial guess P_0. Specifically, for fixed $h = 0.1154$, $\delta = 0$, $\tau = 1/8$, $m = 3000$ and $n = 20$,

Table 5. Dependence of solution accuracy on P_0.

P_0	HM	LMLSM	SQPM	IPM
0	2.4046e−2	2.8239e−2	2.6692e−2	2.4112e−2
0.01	2.4046e−2	2.7739e−2	2.6706e−2	2.7935e−2
0.1	2.4041e−2	2.5275e−2	2.7602e−2	2.8760e−2
1	2.3997e−2	2.4197e−2	3.0401e−2	1.7523e−2
10	2.3552e−2	2.4144e−2	1.4272e−2	2.9554e−2
100	2.0817e−2	2.4136e−2	2.7807e−2	3.6534e−2
1000	2.4984e−2	2.3939e−2	8.3977e−2	1.8355e−1
10,000	7.7530e−2	2.4596e−2	4.1916	35.1026

Table 6. The corresponding computational time (s).

P_0	HM	LMLSM	SQPM	IPM
0	20.44	1.67	35.59	92.34
0.01	20.52	1.55	69.08	130.17
0.1	20.50	1.67	42.11	84.61
1	20.48	1.67	35.36	51.69
10	21.23	1.72	101.38	157.25
100	20.66	1.95	113.30	157.75
1000	20.61	1.91	164.22	152.56
10,000	20.97	1.70	154.61	161.33

set $P_0 = 0, 0.01, 0.1, 1, 10, 100, 1000, 10,000$, respectively, and repeat Algorithm 3.5. The corresponding $\varepsilon = 10^{-4}$ for all P_0. The relative error L2Err in reconstructed approximate solutions and computational time needed are reported in the second columns of Tables 5 and 6. Again, for comparison, the numerical results obtained with LMLSM, SQPM and IPM are also shown in Tables 5 and 6. In LMLSM, $\varepsilon = 10^{-4}$ for all P_0. The optimal regularization parameters in SQPM and IPM corresponding to $P_0 = 0$, 0.01, 0.1, 1, 10, 100, 1000, 10,000 are $\varepsilon = 10^{-2}, 10^{-2}, 10^{-2}, 10^{-1}, 10^{-2}, 10^{-1}, 1, 1$ and $\varepsilon = 10^{-2}, 10^{-1}, 10^{-1}, 10^{-2}, 10^{-1}, 10^{-1}, 1, 10^{-1}$, respectively. We see from Table 5 that all methods give satisfactory reconstructions for a large range of P_0. Compared to standard LMLSM, SQPM and IPM, HM produces better solution accuracy for all P_0, especially for those P_0 of big magnitudes. In conclusion, homotopy method explored in this paper has better behaviour than standard sequential quadratic programming-based method and interior point-based method in both solution accuracy and computational time.

We repeat experiments above for random P_0 (positive) of different magnitudes. Similar conclusions can be drawn. When using the solutions obtained from HM as the initial guesses of SQPM or IPM, we get the combined HM+SQPM or HM+IPM. The corresponding numerical experiments show that using the combined methods could improve slightly the solution accuracy when the magnitude of the initial guess P_0 is small, and could improve largely the solution accuracy when the magnitude of the initial guess P_0 is big. However, we omit the presentation of the numerical results here.

Example 2: In this example, a three-dimensional problem is studied. Specifically, let $\Omega = \{(x, y, z) \in \mathbb{R}^3 \mid x^2 + y^2 < 1, 0 < z < 2\}$. In Ω, set again the diffusion and absorption parameters are $D = 0.2$ and $\mu_a = 0.04$. Place a light source $p_*(x, y, z) = 1 + x + y + z$ in $\Omega_* = \{(x, y, z) \in \Omega \mid (x - 0.5)^2 + (y - 0.5)^2 + (z - 1)^2 \leq 0.2^2\}$. See Figure 2 for a sketch of a mesh. The Neumann data on the boundary Γ is $g_1 = (x^2 + y^2 + z^2)/5$. The

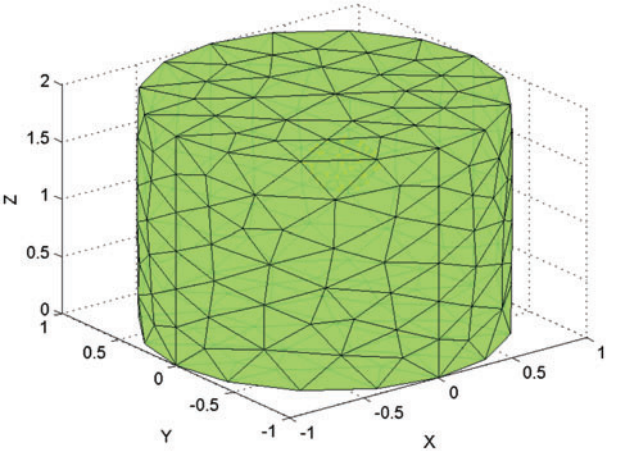

Figure 2. A sketch of mesh of Example 2.

Table 7. Dependence of solution accuracy on parameters τ, m, n.

τ	L2Err	m	L2Err	n	L2Err
1	6.6653e−1	10	1.7291	1	1.3948
1/2	8.3434e−2	50	5.0448e−1	5	1.7689e−1
$1/2^2$	2.0440e−2	100	1.2985e−1	10	2.0408e−2
$1/2^3$	2.0408e−2	150	4.0669e−2	20	5.5481e−2
$1/2^4$	2.0408e−2	200	2.0408e−2	30	9.4306e−2
$1/2^5$	2.0408e−2	250	2.4129e−2	40	1.2606e−1
$1/2^6$	2.0408e−2	300	3.3756e−2	50	1.5171e−1
$1/2^7$	2.0408e−2	350	4.4265e−2	60	1.7248e−1
$1/2^8$	2.0408e−2	400	5.4701e−2	70	1.8942e−1
$1/2^9$	2.0408e−2	450	6.4793e−2	80	2.0337e−1
$1/2^{10}$	2.0408e−2	500	7.4445e−2	90	2.1499e−1
$1/2^{11}$	2.0408e−2	1000	1.4739e−1	100	2.2479e−1

Dirichlet data g_2^δ is computed on a rather fine mesh with $h = 0.1130$, 55,269 nodes and 314,982 elements, and is polluted by a noise with level δ.

With Algorithm 3.5, the approximate source function p^h is recovered on a mesh with $h = 0.2285$, 5023 nodes, 26,885 elements for various values of the parameters δ, ε, τ, m and n. Like Example 1, we first investigate the effect of the smoothing parameter τ, the partition parameter m and the iteration parameter n, on the accuracy of reconstructed approximate solutions. To this end, we fix $\delta = 0, \varepsilon = 10^{-5}$, and set $P_0 = 10$, which is again very different from the true solution p_*. The results are reported in Table 7. Specifically, the relative error L2Err for different values of τ are given in the first two columns (fix $m = 200, n = 10$); those for different values of m are listed in the third and forth columns (fix $\tau = 1/16, n = 10$); those for different values of n are listed in the last two columns (fix $\tau = 1/16, m = 200$). Similar conclusions to those from Table 1 can be drawn from Table 7: a moderately small τ, a moderately big n and a big enough m could produce a reasonable approximation p^h to the true source function p_*. The corresponding computational time needed are given Table 8. As Example 1, using data of Table 8 and applying least square

Table 8. The corresponding computational time (s).

τ	Time (s)	m	Time (s)	n	Time (s)
1	989.30	10	439.69	1	473.83
$1/2^1$	985.64	50	551.39	5	700.59
$1/2^2$	980.78	100	693.19	10	979.04
$1/2^3$	981.75	150	836.95	20	1558.28
$1/2^4$	979.04	200	979.04	30	2126.97
$1/2^5$	983.73	250	1126.06	40	2703.63
$1/2^6$	983.17	300	1275.02	50	3269.58
$1/2^7$	995.70	350	1417.34	60	3851.36
$1/2^8$	984.06	400	1563.75	70	4396.83
$1/2^9$	983.00	450	1691.86	80	4946.31
$1/2^{10}$	981.64	500	1833.42	90	5527.66
$1/2^{11}$	983.09	1000	3257.17	100	6140.36

Table 9. The dependence of solution accuracy on δ.

δ	HM	LMLS	SQPM	IPM
0	2.0408e−2	1.8158e−1	7.0435e−1	1.3598
0.1%	5.2177e−2	2.2587e−1	7.2448e−1	1.3593
0.5%	1.0210e−1	2.3589e−1	7.2496e−1	1.3512
1%	1.3647e−1	2.8666e−1	7.3166e−1	1.3561
5%	4.9844e−1	5.3604e−1	7.4582e−1	1.4000

Table 10. The corresponding computational time (s).

δ	HM	LMLS	SQPM	IPM
0	1757.44	1193.91	7669.42	994.97
0.1%	1038.36	915.66	6473.69	1069.00
0.5%	994.25	779.06	6597.28	1079.03
1%	992.53	843.56	6047.05	1075.64
5%	1001.33	859.33	2670.88	1072.75

fitting, the formula for the dependence of the computational time on the parameters τ, m and n for 3D problem here is approximately:

$$\text{Time}(\tau, m, n) \approx 2.8495m + 56.9560n - 155.2064.$$

Then uniform noise with different noise level δ are added to measurements and Algorithm 3.5 is repeated, for fixed $P_0 = 10$, $h = 0.2285$, $\tau = 1/16$, $m = 200$ and $n = 10$. $\varepsilon = 10^{-5}, 10^{-5}, 10^{-4}, 10^{-5}, 10^{-3}$ for $\delta = 0, 0.1\%, 0.5\%, 1\%, 5\%$. The relative error L2Err and the corresponding computational time are reported in Tables 9 and 10. Again, for comparison, results obtained with methods LMLSM, SQPM and IPM are also listed in the tables. For $\delta = 0, 0.1\%, 0.5\%, 1\%, 5\%$, the approximate optimal values of the regularization parameter in LMLSM, SQPM and IPM are $\varepsilon = 10^{-4}, 10^{-4}, 10^{-3}, 10^{-3}, 10^{-3}$, $\varepsilon = 10^{-2}, 10^{-4}, 10^{-4}, 10^{-5}, 10^{-5}$ and $\varepsilon = 10^{-4}, 10^{-3}, 10^{-1}, 10^{-1}, 10^{-1}$, respectively. Similar observations to those about Example 1 could be found, that is, all methods are stable; homotopy method explored in this paper has better solution accuracy than other three

Table 11. Dependence of solution accuracy on P_0.

P_0	HM	LMLSM	SQPM	IPM
0	3.3071e−2	1.3453e−1	4.1603e−1	2.5748e−1
0.01	3.3044e−2	1.3679e−1	3.8805e−1	8.5559e−1
0.1	3.2800e−2	1.3627e−1	3.8261e−1	4.9938e−1
1	3.0422e−2	1.3452e−1	2.5921e−1	2.6129e−1
10	2.0408e−2	1.8158e−1	7.0435e−1	1.3598
100	1.7783e−1	1.5057e−1	5.4696	18.7512
1000	6.1940e−1	1.4220e−1	1956.99	194.3832
10,000	7.4301	1.4220e−1	1537.96	1956.99

Table 12. The corresponding computational time (s).

P_0	HM	LMLSM	SQPM	IPM
0	933.63	663.59	1352.56	1049.59
0.01	953.08	643.39	1800.44	1043.00
0.1	944.97	649.16	1692.89	1051.94
1	938.44	500.73	1371.94	974.23
10	939.25	1193.91	7669.42	994.97
100	950.67	730.34	15,240.64	1023.09
1000	975.19	1012.69	1000.17	1014.13
10,000	951.80	912.34	1992.22	1000.17

methods; Levenberg–Marquardt based least square method for $\gamma = 0$ is faster than other three methods; HM is faster than SQPM and IPM.

Finally, for the three-dimensional problem, we also assess the convergence behaviour of our homotopy method with respect to initial guess P_0. Specifically, for fixed $h = 0.2285$, $\delta = 0$, $\tau = 1/16$, $m = 200$ and $n = 10$, set $P_0 = 0, 0.01, 0.1, 1, 10, 100, 1000, 10{,}000$, respectively, and repeat Algorithm 3.5. Corresponding to each P_0, $\varepsilon = 10^{-5}, 10^{-5}, 10^{-5}, 10^{-5}, 10^{-5}, 10^{-3}, 10^{-3}, 10^{-2}$. The relative error L2Err and time cost are reported in the second columns of Tables 11 and 12. The numerical results obtained with LMLSM, SQPM and IPM are also shown in Tables 11 and 12. In LMLSM, $\varepsilon = 10^{-4}$ for all P_0 while the optimal regularization parameters in SQPM and IPM corresponding to $P_0 = 0, 0.01, 0.1, 1, 10, 100, 1000, 10{,}000$ are $\varepsilon = 10^{-3}, 10^{-2}, 10^{-2}, 10^{-4}, 10^{-2}, 1, 10^{-3}, 10^{-4}$ and $\varepsilon = 10^{-2}, 10^{-1}, 10^{-2}, 10^{-4}, 10^{-4}, 10^{-3}, 10^{-3}, 10^{-4}$, respectively. Again, we see from Table 11 that all three methods give satisfactory reconstructions for a large range of P_0. Compared to standard LMLSM, SQPM and IPM, HM produces better solution accuracy for not too big P_0. In conclusion, homotopy method explored in this paper has better behaviour in solution accuracy than other three standard methods, and in computational time than SQPM and IPM.

Note that for initial guess P_0 with big magnitude, the results in HM look also not good. we may increase the partition parameter m and outer iteration parameter n to improve the solution accuracy. For instance, for $P_0 = 10{,}000$, when increasing $m = 200$ to $m = 500$, and $n = 10$ to $n = 30$, the L^2-norm relative error decreases from 7.4301 to 7.5078e−1. However, again, for the conciseness of the paper, we omit these results here.

Example 3: Different from Examples 1 and 2, in our last example, a source with multiple disconnected supports is considered. Moreover, for verifying the feasibility of our method, we set the true source being of different magnitudes in different supports. Specifically, let

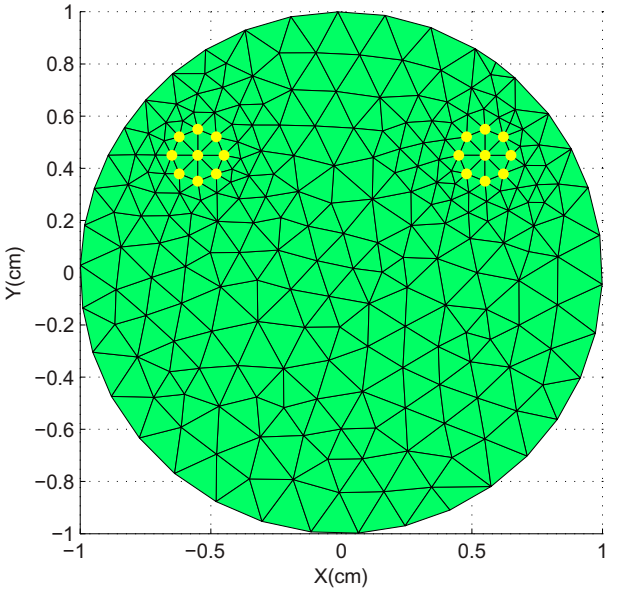

Figure 3. A sketch of Delaunay elements.

Table 13. The dependence of the accuracy in solutions on parameters τ, m, n.

τ	L2Err	m	L2Err	n	L2Err
1	5.1553e−1	200	1.3709e−1	1	1.1602
$1/2^1$	4.9439e−1	400	1.0248e−1	5	1.4851e−1
$1/2^2$	1.3214e−1	600	7.7854e−2	10	1.1082e−1
$1/2^3$	2.2914e−2	800	5.9211e−2	20	6.6953e−2
$1/2^4$	4.3358e−2	1000	4.5091e−2	30	4.0965e−2
$1/2^5$	4.8881e−2	1200	3.4761e−2	40	2.6991e−2
$1/2^6$	5.1049e−2	1400	2.7857e−2	50	2.2914e−2
$1/2^7$	5.1904e−2	1600	2.4088e−2	60	2.4661e−2
$1/2^8$	5.2301e−2	1800	2.2914e−2	70	2.8015e−2
$1/2^9$	5.2488e−2	2000	2.3484e−2	80	3.1213e−2
$1/2^{10}$	5.2571e−2	2200	2.4963e−2	90	3.3837e−2
$1/2^{11}$	NaN	2400	2.6784e−2	100	3.5883e−2

the true source $p_* = 0.1 + x + y$ when $(x, y) \in \Omega_1$ and $p_* = 10 - x + y$ when $(x, y) \in \Omega_2$, where Ω_1 and Ω_2 are circles located at $(0.55, 0.45)$ and $(-0.55, 0.45)$, respectively, both with radius 0.1. The other assumptions about Ω, the diffusion and absorption parameters D and μ_a, the Neumann data g_1 on Γ are the same as Example 1. We show in Figure 3 for a sketch of a computational mesh. Again, the Dirichlet data g_2^δ is computed on a rather small meshsize h ($h = 0.02166$ with 57,769 nodes and 114,944 elements in our experiments), polluted by a noise with level δ.

Using Algorithm 3.5, the approximate source function p^h is recovered on a mesh with $h = 0.1268$, for different parameters $\delta, \varepsilon, \tau, m$ and n. For fixed $\delta = 0, \varepsilon = 10^{-5}$, the effects of τ, m and n on solution accuracy and time cost are shown in Tables 13 and 14. Like Example 1, we set $P_0 = 100$, which is again far from the true solution p_*. The relative

Table 14. The corresponding computational time (s).

τ	Time	m	Time	n	Time
1	195.80	200	24.63	1	7.72
$1/2^1$	192.59	400	46.86	5	22.92
$1/2^2$	193.33	600	67.42	10	44.41
$1/2^3$	192.66	800	88.84	20	83.63
$1/2^4$	193.13	1000	110.61	30	120.80
$1/2^5$	192.00	1200	131.39	40	159.73
$1/2^6$	216.89	1400	153.47	50	200.97
$1/2^7$	190.69	1600	175.03	60	243.52
$1/2^8$	191.02	1800	196.47	70	281.14
$1/2^9$	193.02	2000	217.55	80	326.77
$1/2^{10}$	190.52	2200	238.31	90	360.31
$1/2^{11}$	-	2400	270.47	100	399.98

Table 15. The dependence of solution accuracy on δ.

δ	HM	LMLS	SQPM	IPM
0	2.2914e−2	3.2616e−2	2.1415e−1	4.0153e−1
0.1%	4.0387e−2	6.6006e−2	2.4492e−1	2.6656e−1
0.5%	6.9475e−2	5.1734e−2	2.4077e−1	3.2944e−1
1%	8.0509e−2	1.4799e−1	3.0787e−1	3.7943e−1
5%	1.1496e−1	9.7264e−2	3.3048e−1	5.0110e−1

Table 16. The corresponding computational time (s).

δ	HM	LMLS	SQPM	IPM
0	200.97	2.19	69.56	78.08
0.1%	200.50	2.30	47.95	79.09
0.5%	201.52	2.28	92.77	79.52
1%	197.53	2.14	83.67	83.08
5%	194.36	2.41	98.50	73.09

L^2-norm error L2Err in approximate solutions for different values of τ are given in the first two columns (fix $m = 1800$, $n = 50$); those for different values of m are listed in the third and forth columns (fix $\tau = 1/8$, $n = 50$); those for different values of n are listed in the last two columns (fix $\tau = 1/8$, $m = 1800$). In Table 13, 'NaN' means matrix $\frac{\partial H_\tau}{\partial P}$ in (3.18) is singular and the condition number of it is rather big. The conclusions about the dependence of the solution accuracy and the computational time on parameters τ, m and n in Example 1 hold for the multiple sources considered here. Using data in Table 14 and applying least square fitting, the explicit formula of the computational time with respect to τ, m and n are approximated as follows:

$$\text{Time}(\tau, m, n) \approx 0.1089m + 3.9814n - 200.4765.$$

Set $P_0 = 100$ and $h = 0.1268$, four methods are implemented for $\delta = 0$, 0.1%, 0.5%, 1%, 5% and the results are shown in Tables 15 and 16. In HM, $\tau = 1/8$, $m = 1800$ and $n = 50$, and the approximate optimal regularization parameters corresponding to five different δ are $\varepsilon = 10^{-5}$, 10^{-5}, 10^{-4}, 10^{-4}, 10^{-4}. In LMLSM, SQPM and PDIPM, The

Table 17. Dependence of solution accuracy on P_0.

P_0	HM	LMLSM	SQPM	IPM
0	4.2253e−2	3.4793e−2	2.0635e−1	1.6068e−1
0.01	4.2245e−2	3.4759e−2	2.0683e−1	2.3098e−1
0.1	4.2177e−2	3.4560e−2	2.0566e−1	1.7362e−1
1	4.1504e−2	3.4621e−2	1.8447e−1	1.6107e−1
10	3.5152e−2	3.2616e−2	1.5296e−1	1.0910e−1
100	2.2914e−2	3.2614e−2	2.1415e−1	4.0153e−1
1000	5.7678e−2	3.4853e−2	4.0311e−1	6.9583e−1
10,000	5.7509e−2	3.9699e−2	4.9351e−1	15.7269

Table 18. The corresponding computational time (s).

P_0	HM	LMLSM	SQPM	IPM
0	228.23	3.27	57.47	78.33
0.01	221.80	3.28	62.52	74.55
0.1	222.16	3.23	36.88	80.56
1	220.66	2.20	55.72	67.56
10	192.70	2.17	56.34	80.84
100	213.66	2.23	69.56	78.08
1000	214.14	2.36	166.11	75.45
10,000	213.09	2.41	170.56	78.61

approximate optimal regularization parameters corresponding to different δ are $\varepsilon = 10^{-6}$, $10^{-4}, 10^{-4}, 10^{-4}, 10^{-4}, \varepsilon = 10^{-2}, 10^{-5}, 10^{-8}, 10^{-4}, 10^{-7}$ and $\varepsilon = 10^{-8}, 10^{-8}, 10^{-2}, 10^{-5}$, 10^{-2}, respectively. Again, Table 15 shows that all four methods are stable and can give satisfactory reconstructions. In comparison, homotopy method explored in this paper has better solution accuracy than other three methods for most of δ and Levenberg–Marquardt based least square method is faster than other three methods, while HM is faster than SQPM and IPM.

Finally, for the multiple sources problem, we also consider the dependence of the approximate solutions one initial guess P_0. Specifically, for fixed $h = 0.1268$, $\delta = 0$, $\tau = 1/8, m = 1800$ and $n = 50$, set $P_0 = 0, 0.01, 0.1, 1, 10, 100, 1000, 10{,}000$, respectively, and repeat Algorithm 3.5. Corresponding to each P_0, $\varepsilon = 10^{-10}$, 10^{-10}, 10^{-10}, 10^{-10}, $10^{-15}, 10^{-5}, 10^{-4}, 10^{-4}$. The relative error L2Err and time cost are reported in the second columns of Tables 17 and 18. The numerical results obtained with LMLSM, SQPM and IPM are also shown in Tables 17 and 18. In LMLSM, $\varepsilon = 10^{-6}$ for all P_0 while the optimal regularization parameters in SQPM and IPM corresponding to eight P_0 are $\varepsilon = 10^{-2}, 10^{-2}$, $10^{-4}, 10^{-3}, 10^{-2}, 10^{-2}, 10^{-4}, 10^{-1}$ and $\varepsilon = 10^{-8}, 10^{-9}, 10^{-12}, 10^{-10}, 10^{-8}, 10^{-8}, 10^{-2}$, 10^{-2}, respectively. Again, we see from Table 17 that all three methods give satisfactory reconstructions for a large range of P_0. Table 17 shows both HM and LMLSM have good accuracy, and perform better than standard SQPM and IPM for almost all P_0. In this example, the computational time in HM is more than other three methods. This is because the outer iteration number $n = 50$ is relatively big.

5. Conclusion

BLT is an under-determined inverse source problem and seriously ill-posed. By applying the Tikhonov regularization, the BLT problem is reduced to an optimization problem,

which is further solved with a homotopy method. The main aim of this paper is to explore a method which can provide a reasonable approximate source for a bad initial guess. As shown by theoretical analysis and numerical examples, the homotopy-based method proposed here for the BLT problem is stable and is convergent for a large range of initial guess. Moreover, our numerical experiments above indicate that, compared with standard sequential quadratic programming method and primal-dual interior point method, the CCBM-based homotopy iterative method converges faster and has better solution accuracy.

Acknowledgements

We thank the three anonymous referees for their careful review of our manuscript and for their constructive comments.

Disclosure statement

No potential conflict of interest was reported by the authors.

Funding

The work of the first author was supported partly by the Natural Science Foundation of China [grant number 11401304]; the Natural Science Foundation of Jiangsu Province [grant number BK20130780]; the Fundamental Research Funds for the Central Universities [grant number NS2014078]. The work of the second author was supported partly by the Natural Science Foundation of China [grant number 11571311]. The work of the third author was partly supported by Simons Foundation [grant number 207052], [grant number 228187].

References

[1] Cherry SR. In vivo molecular and genomic imaging: new challenges for imaging physics. Phys Med Biol. 2004;49:13–48.
[2] Levin CS. Primer on molecular imaging technology. Eur J Nucl Med Mol Imaging. 2005;32:325–345.
[3] Massoud TF, Gambhir SS. Molecular imaging in living subjects: seeing fundamental biological processes in a new light. Genes Dev. 2003;17:545–580.
[4] Ray P, Wu AM, Gambhir SS. Optical bioluminescence and bositron emission tomography imaging of a novel fusion reporter gene in tumor xenografts of living mice. Cancer Res. 2003;63:1160–1165.
[5] Troy T, Mcmullen DJ, Sambucetti L, et al. Quantitative comparison of the sensitivity of detection of fluorescent and bioluminscent reporters in animal models. Mol Imaging. 2004;3:9–23.
[6] Bhaumik S, Gambhir SS. Optical imaging of Renilla luciferase reporter gene expression in living mice. Proc Natl Acad Sci USA. 2002;99:377–382.
[7] Contag C, Bachmann MH. Advances in bioluminescence imaging of gene expression. Ann Rev Biomed Eng. 2002;4:235–260.
[8] Kuckuk PM, Boskey AL. Molecular imaging promotes progress in orthopedic research. Bone. 2006;39:965–977.
[9] Blasberg R. Imaging gene expression and endogenous molecular processes: molecular imaging. J Cereb Blood Flow Metab. 2002;22:1157–1164.
[10] Gambhir SS. Molecular imaging of cancer with positron emission tomograph. Nat Rev Cancer. 2002;2:683–693.

[11] Genove G, DeMarco U, Xu H, et al. A new transgene reporter for in vivo magnetic resonance imaging. Nat Med. 2005;11:450–454.
[12] Weissleder R, Ntziachristos V. Shedding light onto live molecular targets. Nat Med. 2003;9:123–128.
[13] Ntziachristos V, Ripoll J, Wang LV, et al. Looking and listening to light: the evolution of whole-body photonic imaging. Nat Biotechnol. 2005;23:313–320.
[14] Ntziachristos V, Tung CH, Bremer C, et al. Fluorescence molecular tomography resolves protease activity in vivo. Nat Med. 2002;8:757–760.
[15] Douraghy A, Prout DL, Silverman RW, et al. Evaluation of scintillator afterglow for use in a combined optical and PET imaging tomograph. Nucl Instrum Methods Phys Res A. 2006;569:557–562.
[16] Loo WTY, Tong JMK, Cheung MNB, et al. A new predictive and prognostic marker (ATP bioluminescence and positron emission tomography) in vivo and in vitro for delivering adjuvant treatment plan to invasive breast tumor patients. Biomed Pharmacother. 2006;60:285–288.
[17] Serganova I, Moroz E, Moroz M, et al. Non-invasive molecular imaging and reporter genes. Cent Eur J Biol. 2006;1:88–123.
[18] Baumjohann D, Lutz MB. Non-invasive imaging of dendritic cell migration in vivo. Immunobiology. 2006;211:587–597.
[19] Cong AX, Wang G. Multispectral bioluminescence tomography: methodology and simulation. Int J Biomed Imaging. 2006;2006:Article ID 57614, 7 p.
[20] Chaudhari AJ, Darvas F, Bading JR, et al. Hyperspectral and multispectral bioluminescence optical tomography for small animal imaging. Phys Med Biol. 2005;50:5421–5441.
[21] Doyle TC, Burns SM, Contag CH. In vivo bioluminescence imaging for integrated studies of infection. Cell Microbiol. 2004;6:303–317.
[22] Li SH, Driessen W, Sullivan S, et al. Bioluminescence tomography based on phantoms with different concentrations of bioluminescent cancer cells. J Opt A: Pure Appl Opt. 2006;8:743–746.
[23] Hielscher AH. Optical tomographic imaging of small animals. Curr Opin Biotechnol. 2005;16:79–88.
[24] Alexandrakis G, Rannou FR, Chatziioannou AF. Tomographic bioluminescence imaging by use of a combined optical-PET (OPET) system: a computer simulation feasibility study. Phys Med Biol. 2005;50:4225–4241.
[25] Han W, Cong WX, Wang G. Mathematical theory and numerical analysis of bioluminescence tomography. Inverse Probl. 2006;22:1659–1675.
[26] Han W, Cong WX, Wang G. Mathematical study and numerical simulation of multispectral bioluminescence tomography. Int J Biomed Imaging. 2006;2006:Article ID 54390, 10 p.
[27] Han W, Wang G. Theoretial and numerical analysis on multispectral boluminescence tomography. IMA J Appl Math. 2007;72:67–85.
[28] Natterer F, Wabbeling F. Mathematical methods in image reconstruction. Philadephia (PA): SIAM; 2001.
[29] Cong WX, Durairaj K, Wang LV, et al. A Born-type approximation method for bioluminescence tomography. Med Phys. 2006;33:679–686.
[30] Cong WX, Wang G, Kumar D, et al. Practical reconstruction method for bioluminescence tomography. Opt Express. 2005;13:6756–6771.
[31] Lv Yj, Tian J, Cong WX, et al. A multilevel adaptive finite element algorithm for bioluminescence tomography. Opt Express. 2006;14:8211–8223.
[32] Cheng XL, Gong RF, Han W, et al. A novel coupled complex boundary method for solving inverse source problems. Inverse Probl. 2014;30:055002.
[33] Watson LT. globally convergent homotopy methods: a tutorial. Appl Math Comput. 1989;31:369–396.
[34] Dautray R, Lions JL. Mathematical analysis and numerical methods for science and technology. Vol. 2. Berlin: Springer; 1988.

[35] Gong RF, Cheng XL, Han W. A new coupled complex boundary method for bioluminescence tomography. Commun Comput Phys. 2016;19:226–250.
[36] Cottle RW, Pang JS, Stone RE. The Linear complementarity problem. Boston (MA): Academic Press; 1992.
[37] Harker PT, Pang JS. Finite-dimensional variational inequality and nonlinear complementarity problem: a survey of theory, algorithm and applications. Math Program. 1990;48:161–220.
[38] Chen CH, Mangasarian OL. A class of smoothing functions for nonlinear and mixed complementarity problems. Comput Optim Appl. 1996;5:97–138.
[39] Fan XN, Yu B. Homotopy method for solving variational inequalities with bounded box constraints. Nonlinear Anal. 2008;68:2357–2361.
[40] Barrett R, Berry M, Chan TF, et al. Templates for the solution of linear systems: building blocks for iterative methods. Philadelphia (PA): SIAM; 1994.
[41] Hämarik U, Palm R, Raus T. A family of rules for parameter choice in Tikhonov regularization of ill-posed problems with inexact noise level. J Comput Appl Math. 2012;236:2146–2157.
[42] Hansen PC. Analysis of discrete ill-posed problems by means of the L-curve. SIAM Rev. 1992;34:561–580.

Appendix 1. The forms of matrix M and vector N

Let n be the number of nodes of the triangulation $\mathcal{T}_h$ and $\varphi_i(x) \in V^h$ be the nodal basis functions of V^h associated with grid nodes x_i, $1 \le i \le n$. Then finite element solutions, denoted by u^h, w^h, of (2.1) and (2.4) have the forms as follows:

$$u^h = \sum_{i=1}^{n} u_i \varphi_i, \quad w^h = \sum_{i=1}^{n} w_i \varphi_i.$$

Denote by u_{i1}, u_{i2} the real and imaginary parts of u_i, w_{i1}, w_{i2} the real and imaginary parts of $w_i, 1 \le i \le n$, and set $U_1 = (u_{11}, u_{21}, \ldots, u_{n1})^t$, $U_2 = (u_{12}, u_{22}, \ldots, u_{n2})^t$, $U = (U_1^T, U_2^T)^t$, $W_1 = (w_{11}, w_{21}, \ldots, w_{n1})^t$, $W_2 = (w_{12}, w_{22}, \ldots, w_{n2})^t$, $W = (W_1^T, W_2^T)^t$. Moreover, define

$$\begin{aligned}
&A = (a_{ij})_{n\times n}, \quad a_{ij} = \int_\Omega (D\,\nabla\varphi_i \cdot \nabla\varphi_j + \mu_a \varphi_i\,\varphi_j)\,\mathrm{d}x,\\
&B = (b_{ij})_{n\times n}, \quad b_{ij} = \int_\Omega \varphi_i\,\varphi_j\,\mathrm{d}x,\\
&C = (c_{ij})_{n\times n}, \quad c_{kl} = \int_\Gamma \varphi_i\,\varphi_j\,\mathrm{d}s,\\
&R = (r_{ik})_{n\times n_0}, \quad r_{ik} = \int_{T_k} \varphi_i\,\mathrm{d}x,\\
&\tilde{B} = (\tilde{b}_{ki})_{n_0\times n}, \quad \tilde{b}_{ki} = \begin{cases} 1/3, & x_i \in T_k,\\ 0, & \text{otherwise,}\end{cases}\\
&b_1 = (b_{1,i})_{n\times 1}, \quad b_{1,i} = \int_\Gamma g_1^\delta \varphi_i\,\mathrm{d}s\\
&b_2 = (b_{2,i})_{n\times 1}, \quad b_{2,i} = \int_\Gamma g_2^\delta \varphi_i\,\mathrm{d}s.
\end{aligned}$$

and set

$$L = \begin{bmatrix} A & -C \\ C & A \end{bmatrix}, \quad K_1 = \begin{bmatrix} R \\ 0_{n\times n_0} \end{bmatrix}, \quad K_2 = \begin{bmatrix} B \\ 0_{n\times n} \end{bmatrix}, \quad b = [b_1^t,\, b_2^t]^t.$$

Then the dicretization $\mathbf{f}$ of f, from $\mathbb{R}^{n_0}$ to $\mathbb{R}^{n_0}$, has the form

$$\mathbf{f}(P) = \tilde{B}\,W_2 + \varepsilon P \tag{A1}$$

with W_2 satisfying

$$L\,U = K_1\,P + b, \tag{A2}$$

$$L\,W = K_2\,U_2. \tag{A3}$$

(A2) and (A3) are the reduced systems of algebraic equations obtained from the finite element dicretization of (2.1) and (2.4). Substitute them into (A1) to give formally

$$\begin{aligned}\mathbf{f}(P) &= \left[\tilde{B}(A+CA^{-1}C)^{-1}CA^{-1}B(A+CA^{-1}C)^{-1}CA^{-1}R+\varepsilon D_0\right]P\\ &\quad+\tilde{B}(A+CA^{-1}C)^{-1}CA^{-1}B(A+CA^{-1}C)^{-1}(CA^{-1}b_1-b_2)\\ &\triangleq MP+N,\end{aligned}$$

where D_0 is a $n_0 \times n_0$ diagonal matrix with $D_{0,kk} = |T_k|$, the measure of element T_k, $1 \le k \le n_0$.